Editors' Suggestion

# Magnetization dynamics affected by phonon pumping

Richard Schlitz,[1,2,*] Luise Siegl,[3,2] Takuma Sato,[4] Weichao Yu,[5,6,4] Gerrit E. W. Bauer,[4,7,8] Hans Huebl,[9,10,11] and Sebastian T. B. Goennenwein[3,2]

[1]*Department of Materials, ETH Zürich, 8093 Zürich, Switzerland*
[2]*Institut für Festkörper- und Materialphysik, Technische Universität Dresden and Würzburg-Dresden Cluster of Excellence ct.qmat, 01062 Dresden, Germany*
[3]*Department of Physics, University of Konstanz, 78457 Konstanz, Germany*
[4]*Institute for Materials Research, Tohoku University, Sendai 980-8577, Japan*
[5]*State Key Laboratory of Surface Physics and Institute for Nanoelectronic Devices and Quantum Computing, Fudan University, Shanghai 200433, China*
[6]*Zhangjiang Fudan International Innovation Center, Fudan University, Shanghai 201210, China*
[7]*AIMR and CSRN, Tohoku University, Sendai 980-8577, Japan*
[8]*Zernike Institute for Advanced Materials, Groningen University, Groningen, The Netherlands*
[9]*Walther-Meißner-Institut, Bayerische Akademie der Wissenschaften, 85748 Garching, Germany*
[10]*Physik-Department, Technische Universität München, 85748 Garching, Germany*
[11]*Munich Center for Quantum Science and Technology (MCQST), 80799 München, Germany*

(Received 4 February 2022; revised 14 June 2022; accepted 21 June 2022; published 11 July 2022)

"Pumping" of phonons by a dynamic magnetization promises to extend the range and functionality of magnonic devices. We explore the impact of phonon pumping on room-temperature ferromagnetic resonance (FMR) spectra of bilayers of thin yttrium iron garnet films on thick gadolinium gallium garnet substrates over a wide frequency range. At low frequencies the Kittel mode hybridizes with standing ultrasound waves across the layer stack that acts as a bulk acoustic resonator to form magnon polarons with rapid oscillations in the magnetic susceptibility, as reported before. At higher frequencies, the individual phonon resonances overlap due to their increasing acoustic attenuation, leading to an additional slowly oscillating phonon pumping contribution to the FMR line shape. The broadband frequency dependence of the magnetoelastic coupling strength follows the predictions from phonon pumping theory in the thick substrate limit. In addition, we find substantial magnon-phonon coupling of a perpendicular standing spin wave mode. This evidences the importance of the mode overlap between the acoustic and magnetic modes and provides a route towards engineering the magnetoelastic mode coupling.

DOI: 10.1103/PhysRevB.106.014407

## I. INTRODUCTION

Magnons and phonons are, respectively, the elementary excitations of the magnetic and atomic order in condensed matter. They are coupled by weak magnetoelastic and magnetorotational interactions, which can often simply be disregarded. However, recent experimental and theoretical research reveals that the magnon-phonon interaction may cause spectacular effects in (i) ferromagnets close to a structural phase transition such as Galfenol [1,2] or (ii) magnets with exceptionally high magnetic and acoustic quality such as yttrium iron garnet [3–9].

Magnons are promising carriers for future low-power information and communication technologies [10,11]. The magnon-phonon interaction can benefit the functionality of magnonic devices by helping to control and enhance magnon propagation when coherently coupled into magnon polarons [4,9]. On the other hand, magnon nonconserving magnon-phonon scattering is the main source of magnon dissipation at room temperature [12,13].

The study of magnon-phonon interactions in high-quality magnets has a long history [14–21]. The arrival of crystal growth techniques, strongly improved microwave technology, and discovery of new phenomena such as the spin Seebeck effect led to a revival of the subject in the past few years, with emphasis on ultrathin films and heterostructures [4,6,22–30].

High-quality yttrium iron garnet (YIG) is an excellent material to study magnons and phonons. Thin films grow best on single-crystal substrates of gadolinium gallium garnet (GGG), a paramagnetic insulator that is magnetically inert at elevated temperatures. However, the acoustic parameters of GGG are almost identical to YIG such that phonons are not localized to the magnet and thus the substrate cannot be simply disregarded. Streib *et al.* [3] pointed out that magnetic energy can leak into the substrate by magnon-phonon coupling by a process called "phonon pumping" and predicted that it should cause an increased magnetization damping with a characteristic nonmonotonous dependence on frequency.

Phonon pumping has been experimentally observed in the ferromagnetic resonance of YIG films on GGG substrates

*richard.schlitz@mat.ethz.ch

 

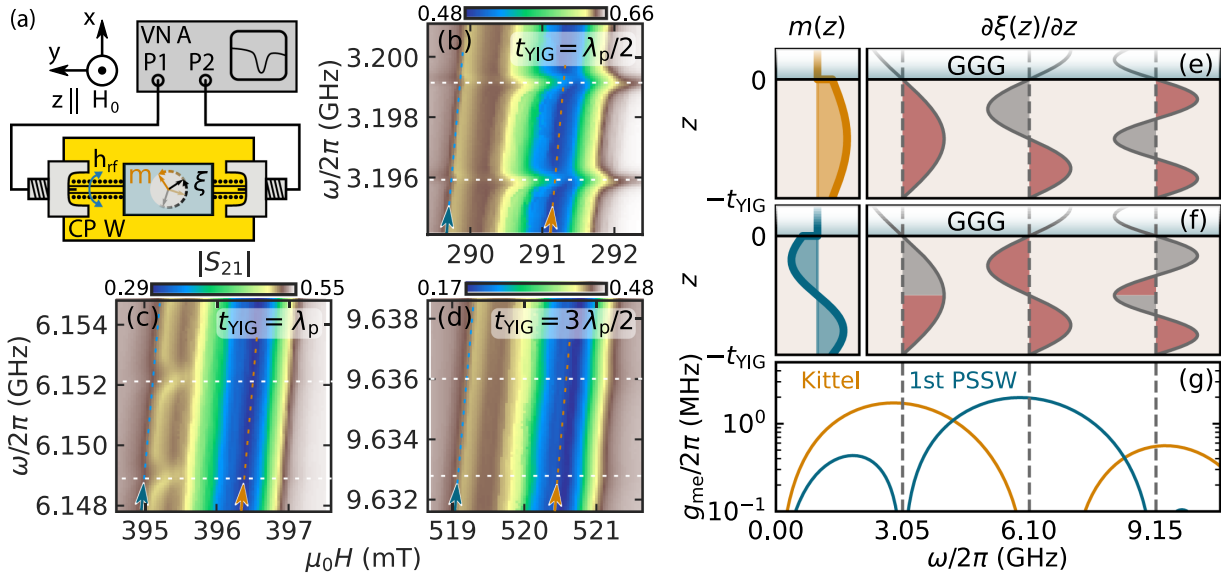


FIG. 1. (a) Thin YIG film on a thick paramagnetic GGG substrate (gray square) placed face down on a coplanar waveguide. The latter is connected to a vector network analyzer to obtain the transmission parameter $S_{21}$ as a function of frequency $\omega$. The external static magnetic field $H_0$ is applied normal to the surface. (b)–(d) High resolution maps of $|S_{21}|$ for different $\omega$ and $H_0$. Shear waves with sound velocity $c_t$ and wavelength $\lambda_p$ form standing waves across the full layer stack. The three panels correspond to $t_{YIG} \sim \lambda_p/2$, $\lambda_p$, and $3\lambda_p/2$, respectively. The fundamental (Kittel) mode and the first perpendicular standing spin wave (PSSW) are marked with orange and blue dashed lines and arrows, respectively. (e), (f) Thickness dependence of the amplitude $m_l(z)$ of the Kittel mode (e) and the first PSSW (f) in the YIG film for $p = 0.5$, plotted together with the eigenmodes of the acoustic strain $\partial\xi(z)/\partial z$ by the phonons at the frequencies of panels (b)–(d). The overlap integral of the modes determines the magnetoelastic coupling strength. The partial cancellation of positive and negative contributions as shaded in red and gray, respectively, strongly depends on the mode numbers and frequency. The magnetic excitation and thus the mode overlap vanishes in the GGG layer, whereas the phonons extend across full YIG/GGG sample stack. (g) The obtained magnetoelastic coupling strength $g_{me}$ shows characteristic oscillations.

[4,29,30]. These experiments revealed coherent hybridization of the (uniform) Kittel magnon with standing sound waves extended over the whole sample. In YIG/GGG/YIG trilayers phonon exchange couples magnons dynamically over mm distances [4,9]. However, the predicted increased damping due to phonon pumping and the coupling of other than the macrospin Kittel magnon remains elusive. The direct detection of the increased damping is challenging due to the presence of inhomogeneous FMR line broadening and the resulting changes of the resonance line shape, in particular in the low frequency regime for thin films [31] or due to the presence of several modes in the resonance for thicker YIG films [32–35].

In this article, we report FMR spectra of YIG/GGG bilayers over a large frequency range, demonstrating the coupling of magnons and phonons from the high cooperativity to the weak coupling regime. We reproduce the magnon polaron fine structure at low frequencies [4,29] and evidence the presence of a broadband emission of phonons at higher frequencies, in line with the acoustic spin pumping effect on the magnetic dissipation predicted in Ref. [3]. The excellent agreement with an analytical model allows us to extract the parameters for the phonon pumping by the (even) Kittel mode in the high cooperativity regime and provides insights into the strong-weak coupling regime at higher frequencies. In addition, we observe that the magnon-phonon coupling strength also is characteristically modulated for an (odd) perpendicular standing spin wave mode. This shows that the overlap integral between magnon and phonon modes governs the coupling strength, thus opening a pathway for controlling it.

## II. EXPERIMENTAL METHODS

Our sample consists of a 630 nm $Y_3Fe_5O_{12}$ film grown by liquid phase epitaxy on a 560 μm thick $Gd_3Ga_5O_{12}$ substrate, which is glued onto a coplanar waveguide (CPW) with a central conductor of width $w = 110$ μm. It is inserted into the air gap of an electromagnet with surface normal parallel to the magnetic field [cf. Fig. 1(a)]. We improve the magnetic field resolution to the 1 μT range by an additional Helmholtz coil pair in the pole gap of the electromagnet that is biased with a separate power supply. We measure the complex microwave transmission spectra $S_{21}(\omega)$ by a vector network analyzer for a series of fixed magnetic field strengths over a large frequency interval at room temperature. An applied microwave power of $P = +5$ dBm gives good signal to noise ratio in the linear regime (see Appendix D).

## III. RESULTS AND DISCUSSION

### A. Broadband ferromagnetic resonance

We first address $S_{21}(\omega)$ in the high cooperativity regime [4] in the form of $|S_{21}|$ as a function of magnetic field and frequency; see Fig. 1(b). The FMR reduces the transmission, emphasized by blue color and centered at the dashed orange line. Periodic perturbations in the FMR at fixed frequencies

with period of ∼3.2 MHz (dashed white lines) correspond to the acoustic free spectral range of the sample

$$\frac{\Delta\omega_p}{2\pi} \approx \frac{c_t}{2t_{GGG}} \sim 3.2\,\mathrm{MHz}, \tag{1}$$

where $c_t = 3570\,\mathrm{ms}^{-1}$ is the transverse sound velocity of GGG [36]. These are the anticrossings of the FMR dispersion with field-independent standing acoustic shear wave modes across the full YIG/GGG layer stack [4,29,30,37,38]. Assuming that the suppression of $|S_{21}|^2$ corresponds to a power transfer from photons into phonons, we estimate an atomic displacement amplitude of 1.7 pm in our experiments (see Appendix C for details). In Fig. 1(b) we additionally observe a resonance corresponding to the PSSW (dashed blue line) shifted to a lower magnetic field by exchange splitting $\mu_0\Delta H = D\pi^2/t_{YIG}^2 \sim 1.4\,\mathrm{mT}$, where $D = 5\times10^{-17}\,\mathrm{Tm}^2$ is the exchange stiffness of YIG [32–35], but without visible coupling to the phonons.

At 6.15 GHz [cf. Fig. 1(c)] the periodic anticrossings vanish for the Kittel mode resonance, which implies a strongly suppressed magnon-phonon coupling. In contrast, the PSSW now exhibits clear anticrossings similar to that of the Kittel mode in panel (b). Increasing the frequency further [cf. Fig. 1(d)] to around 9.63 GHz, the periodic oscillations in the PSSW vanish again, but the anticrossings of the Kittel mode do not recover.

We interpret the suppression of the magnon polaron signal at higher frequencies around 9 GHz in terms of a transition from the (underdamped) high cooperativity [4] to the (overdamped) weak coupling regime. In the latter, the different phonon modes overlap, leading to a broadband contribution of the phonon pumping to the magnon line shape. As a consequence, the periodic magnon polaron signatures vanish in favor of a slowly varying additional broadening of the FMR line that was predicted theoretically in the limit of thick GGG substrates [2,3]. FMR spectra for thicker YIG films show similar features and are displayed in Appendix E.

### B. Theoretical model

The coupling between the elastic and the magnetic subsystems in a confined magnet scales with the overlap integral of the phonon and magnon modes [3,29]. The profile of a PSSW with index $l$ can be modeled by

$$m_l(z) = p\,\sin\left([l+1]\pi[z+t_{YIG}]/t_{YIG}\right) + (1-p)\cos\left(l\pi[z+t_{YIG}]/t_{YIG}\right), \tag{2}$$

where $z \in [-t_{YIG}, 0]$ and $0 \leqslant p \leqslant 1$ interpolates between free ($p = 0$) and pinned ($p = 1$) surface dynamics. Assuming free elastic boundary conditions, a shear wave across the full layer stack with amplitude $\xi$ and frequency $\omega$ creates a strain profile (disregarding the standing wave formation and thus the finite free spectral range) in the YIG film that is given by

$$\frac{\partial\xi(z)}{\partial z} = \frac{\omega}{\widetilde{c}_t}\sin\frac{\omega(t_{YIG}+z)}{\widetilde{c}_t}, \tag{3}$$

where $\xi(z)$ is the local displacement and $\widetilde{c}_t = 3843\,\mathrm{ms}^{-1}$ is the transverse sound velocity of YIG. Note that the ladder of modes is disregarded here for simplicity. The overlap integral of the fundamental (Kittel) mode with $l = 0$ [Fig. 1(e)] and the first PSSW with $l = 1$ [Fig. 1(f)] enters the interaction magnetoelastic coupling $g_{me}$ as [29]

$$g_{me,l} = \sqrt{\frac{2b^2\gamma}{\omega\rho M_s t_{GGG} t_{YIG}}}\left|\int_{-t_{YIG}}^{0} m_l(z)\frac{\partial\xi(z)}{\partial z}dz\right|, \tag{4}$$

where the parameters for YIG at room temperature are the magnetoelastic coupling constant $b = 7\times10^5\,\mathrm{J/m}^3$, the mass density $\rho = 5.1\,\mathrm{g/cm}^3$, the gyromagnetic ratio $\gamma/2\pi = 28.5\,\mathrm{GHz\,T}^{-1}$, and the saturation magnetization $M_s = 143\,\mathrm{kAm}^{-1}$ [4]. $g_{me,0}$ and $g_{me,1}$ in Fig. 1(g) for $p = 0.5$ (yellow and blue lines, respectively) reveal differences in the magnetoelastic coupling of the different magnetic modes. In both cases the coupling oscillates as a function of frequency, but the maxima for $l = 0$ and $l = 1$ are shifted by $l\cdot\widetilde{c}_t/2t_{YIG} \approx 3\,\mathrm{GHz}$. Note that this is true also for the higher standing spin wave modes, so that, even at high frequencies, strong magnon-phonon interactions can be realized. In other materials the results may depend on the details of the interface and surface boundary conditions [23]. Here, we focus on magnetic fields perpendicular to the surface in which the magnetoelastic coupling to the longitudinal phonons vanishes [2].

A phonon and a magnon mode with discrete frequencies $\omega_p$ and $\omega_m$ [$= \gamma\mu_0(H - M_{eff})$ for the Kittel mode] and amplitudes $A_p$ and $A_m$, respectively, behave as two harmonic oscillators coupled by the interaction $g_{me}$ [4]:

$$-A_m[\gamma_m + i(\omega_m - \omega)] - iA_p g_{me}/2 + \eta = 0, \tag{5}$$

$$-A_p[\gamma_p + i(\omega_p - \omega)] - iA_m g_{me}/2 = 0, \tag{6}$$

where $\gamma_m$ and $\gamma_p$ are the decay rates (in angular frequency units). $\eta$ parametrizes the coupling of the magnetic order to the external microwaves at frequency $\omega$; see Fig. 2(a). The solution for the magnetic amplitude is

$$A_m = \eta\left[\left(\frac{g_{me}}{2}\right)^2\frac{1}{\gamma_p + i(\omega_p - \omega)} + [\gamma_m + i(\omega_m - \omega)]\right]^{-1}. \tag{7}$$

This resonator couples to a CPW according to [39]

$$S_{21}(\omega) = a\,\exp(i\alpha)\exp(-i\tau\omega)[1 - A_m], \tag{8}$$

in which the first part in the square brackets represents the external circuit with frequency-dependent amplitude and phase shift $a$ and $\alpha$, respectively, and $\tau$ is an electronic delay time. We can fit the unknown parameters $\eta$ and $g_{me}$ to the observed spectra in Figs. 2(b) and 2(c). $\eta$ can be extracted from the amplitude of the ferromagnetic resonance by solving $h_m = |S_{21}(\omega = \omega_m)_{\eta=0}| - |S_{21}(\omega = \omega_m)_{g_{me}=0}| \equiv f(\eta)$. Similarly, the data for a phonon resonance $h_p = |S_{21}(\omega = \omega_p)_{g_{me}=0}| - |S_{21}(\omega = \omega_p)| \equiv g(g_{me})$ can be solved for $g_{me}$. $h_p$ and $h_m$ can be extracted from fits to the experimental data.

### C. Fitting procedure

We fit the Kittel mode lines in $|S_{21}(\omega)|$ at different fixed magnetic fields by a Gaussian to distill the resonance frequency $\omega_m$, the amplitude $h_m$, and width $\gamma_m$ [cf. Fig. 2(b)].

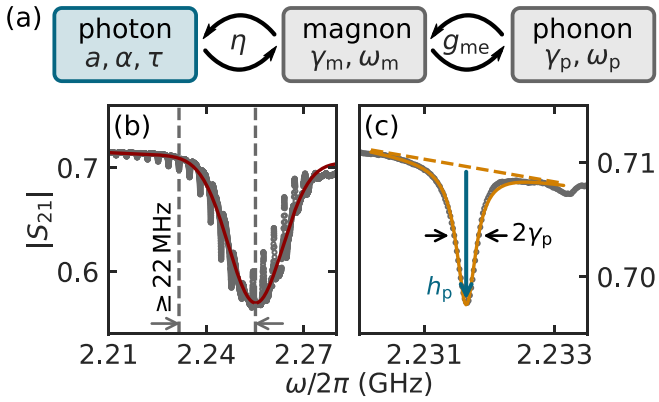


FIG. 2. (a) Phonons and magnons in YIG/GGG bilayers form a two-partite system that can be modeled as coupled harmonic oscillators that are driven by microwave photons [4]. The parameters are the resonance frequencies $\omega_m, \omega_p$, damping constants $\gamma_m, \gamma_p$, and coupling strength $g_{me}$. The coplanar waveguide with transmission amplitude $a$, phase $\alpha$, and electric length $\tau$ interacts with the magnon system parametrized by the coupling strength $\eta$. (b) $|S_{21}|$ as a function of the frequency for $\mu_0 H \approx 259\,\mathrm{mT}$. A Gaussian fit (red line) determines the FMR frequency $\omega_m$ (right dashed line). (c) Zoom-in on the phonon line with $\omega_m - \omega_p = 22\,\mathrm{MHz}$ [marked by the left dashed line in panel (a)]. We obtain the linewidth $\gamma_p$ and the amplitude $h_p$ of the phonon resonance by a Lorentzian fit.

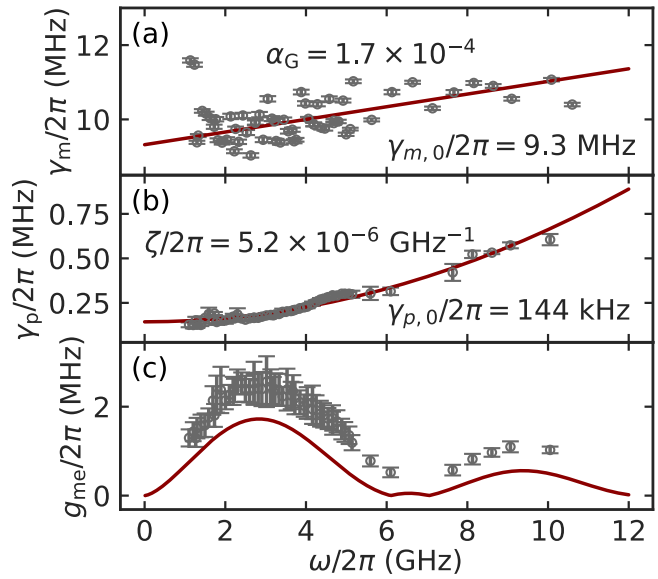


FIG. 3. (a) Half width at half maximum (HWHM) obtained from Gaussian fits to the FMR lines. (b) HWHM from the Lorentzian fits to the acoustic resonances. (c) Magnetoelastic mode coupling obtained from the harmonic oscillator model using the parameters from the fits shown in (a), (b) and in Appendix B. The maximum coupling strength is ∼2.2 MHz.

A good fit by a Gaussian line shape indicates inhomogeneous broadening of the FMR; see below. Next, we select an acoustic resonance at a frequency $\omega_{p,0}$ with $(\omega_m - \omega_{p,0})/2\pi > 2\gamma_m/2\pi \approx 22\,\mathrm{MHz}$, which is only weakly perturbed by the magnon-phonon coupling, but still has a significant oscillator strength. For a better statistics, we independently fit a total of six phonon resonances with frequencies below $\omega_{p,0}$ by Lorentzians [cf. Fig. 2(c)] to extract their average height $h_p$ and broadening $\gamma_p$.

The resulting fit parameters are summarized in Fig. 3 and in Fig. 6. To establish the dynamic magnetic quality of the sample, we first show the linewidth of the FMR $\gamma_m = \gamma_{m,0} + \alpha_G \omega$ in panel (a). It is dominated by an inhomogeneous broadening $\gamma_{m,0}/2\pi = 9.3\,\mathrm{MHz}$ contribution, which we associate to variations of the local (effective) magnetization over the 6 mm long sample and across the thickness profile. We observe a Gilbert damping $\alpha_G \sim 1.7 \times 10^{-4}$ that is larger by a factor of 3 compared to the best LPE films with similar thickness [40,41]. We speculate that this is due to inhomogeneities across the large driven volume, leading to the presence of a manifold of lines which inhibits the unambiguous extraction of the intrinsic linewidth (see further discussion in Appendix D). A linear increase of the linewidth with frequency signals conventional Gilbert damping behavior associated with two and more magnon-magnon and magnon-phonon scattering [12]. An oscillating contribution caused by the magnetoelastic coupling to the standing acoustic waves is relatively small and difficult to observe directly, as will be discussed later.

The acoustic attenuation exhibits a parabolic increase $\gamma_p = \zeta\omega^2 + \gamma_{p,0}$ [cf. Fig. 3(b)], which we associate to scattering with thermal phonons in GGG [42–44]. The inhomogeneous phonon linewidth $\gamma_{p,0}/2\pi = 144\,\mathrm{kHz}$ may be caused by a small angle ∼1° between the bottom and top surfaces of our sample [45], where the estimate is based on the phonon mean free path $\delta \sim c_t/\gamma_p \approx 4\,\mathrm{mm}$ [4]. We do not observe a larger scale disorder in the substrate thickness that would contribute a term $\propto\omega$ to the attenuation [43].

In the lower frequency regime $\omega/2\pi \lesssim 10\,\mathrm{GHz}$ the phonon mean free path $\delta > 1\,\mathrm{mm}$ is larger than twice the thickness of the bilayer. At frequencies above 10 GHz, however, we enter the crossover regime between high cooperativity and weak coupling in which the phononic free spectral range approaches its attenuation ($\Delta\omega_p \sim 2\gamma_p$) and the magnetoelastic coupling strength $g_{me}$. The fitting with individual phonon lines becomes increasingly inaccurate in this regime, as the baseline of the FMR signal without contributions due to phonons cannot be established from the data. In turn, the overlapping phonon lines give rise to a constant coupling between magnons and phonons in addition to the rapidly oscillating contributions, which we will evidence in the next subsection. The oscillations observed in the magnetoelastic mode coupling $g_{me}$ in panel 3(c) agree well with the model Eq. (4) (red line) for a YIG film with a thickness of $t_{YIG} = 630\,\mathrm{nm}$ and a pinning parameter $p = 0.5$ [from Fig. 1(g)]. An alternative assessment based on a full fit of the experiments by the coupled equations for the complex scattering parameter leads to a similar $g_{me}/2\pi = 1.6\,\mathrm{MHz}$ at $\omega/2\pi \approx 2.2\,\mathrm{GHz}$ (see Appendix A). The model likely overestimates the coupling strength, since the inhomogeneous contributions to the line broadening are not considered independently here.

### D. Weak coupling regime

To strengthen our point that the individual phonon lines overlap and give rise to a broadband emission of phonons

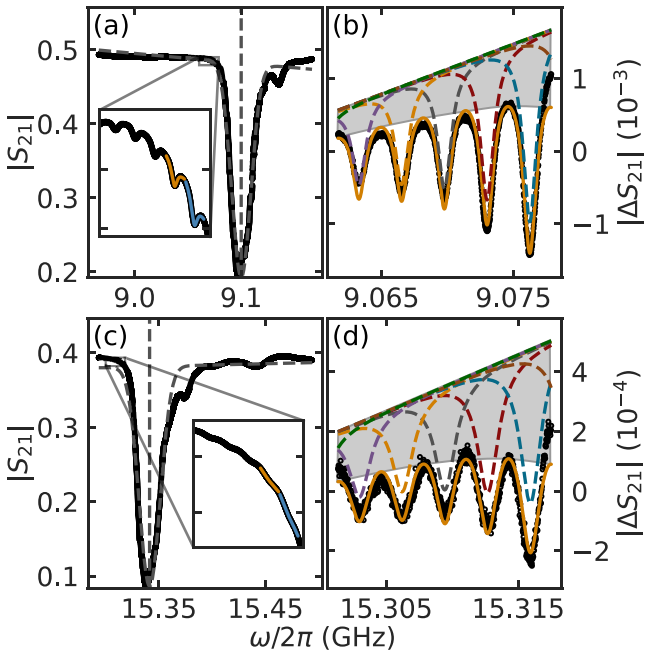


FIG. 4. (a), (c) $|S_{21}(\omega)|$ taken at two constant external magnetic fields corresponding to FMR frequencies around 9 GHz and 15 GHz. The inset shows the region from which the magnetoelastic coupling is evaluated as well as the first two fits' phonon peaks also shown in the main text. (b), (d) The curving background of the data shown in the inset is removed by a polynomial fit and the data is subsequently fitted by a set of several Lorentzian lines with a constant frequency spacing superposed on a linear varying background (solid yellow line). The dashed lines represent the individual Lorentzian components of the fit superimposed on the linear background. The shaded region corresponds to the coupling contribution that does not oscillate with frequency, i.e., is always present.

by the magnetoelastic coupling, we present more detailed data in Fig. 4. Panel (a) depicts an FMR measurement taken around 9 GHz and the inset shows the region used to extract the magnetoelastic coupling including the two Lorentzian fits (see also Fig. 2). To remove background variations due to the FMR signal and thus isolate the phonon contribution to $S_{21}$, we subtract a polynomial from the fitted region [see panel (b)]. The resulting trace is then fit with a manifold of equally spaced Lorentzian lines superposed on a linear background. To limit the number of fit parameters, we assumed a Lorentzian amplitude decay with the detuning from the FMR and used an identical width for all lines. The spacing was fixed at $\Delta\omega_p = 3.233$ MHz. This results in a total of six fit parameters (amplitude, amplitude decay, width, position of the rightmost line, offset, and slope of the linear background). The resulting fit is shown as the solid yellow line, where the individual Lorentzian contributions are represented by dashed lines. The nonoscillatory contribution is shaded gray and corresponds to a constant emission of phonons.

Applying the same evaluation to a FMR spectrum taken at around 15 GHz, two things can be noticed [see Figs. 4(c) and 4(d)]. First, the variation of the microwave absorption is reduced at this higher frequency, as expected from the theoretical trend for the magnetoelastic coupling strength (see Fig. 3). Secondly, the oscillation now appears sinusoidal, contrasting the data at 9 GHz where the dips in the data have an anharmonic shape. This stems from the increased linewidth of the individual phonon resonance ($\gamma_p \sim 0.95$ MHz), which is additionally almost twice the value obtained from the individual fits ($\gamma_p \sim 0.49$ MHz). These data hence represent the weak coupling regime, since $g_{me} \sim 0.7\,\text{MHz} < \gamma_p, \gamma_m$. The large error in the extracted parameters illustrates the limitations of the automatic fitting approach described above, but nevertheless corroborates the physical picture. In particular, the constant contribution (shaded gray area) is enhanced compared to the oscillating part, in line with the expectation for the thick substrate limit, where the fast oscillations are absent [3]. Our data thus corroborate the presence of phonon emission in the weak coupling limit, that depends only on the magnetoelastic coupling strength and thus varies slowly in frequency [see Fig. 3(c)]. From this observation, we conclude that, in the thick substrate limit, the magnetoelastic coupling gives rise to the additional linewidth broadening predicted in Ref. [3].

Magnetization damping in YIG has been extensively studied in the past. However, the oscillating contribution by phonon pumping escaped observation because the magnetoelastic strength is relatively small [see Fig. 3(c)] [3] with a maximum of ∼2.2 MHz, corresponding to a linewidth modulation of 90 μT. This is the typical noise level in most broadband techniques, while inhomogeneous broadening further complicates a direct measurement. Nevertheless, while experiments that are sensitive to only a small volume of the YIG film might still enable a direct measurement of the linewidth broadening, their challenging nature highlights the strength of the method outlined above. The coupling strength extracted from the line shapes can be unambiguously traced to originate from the magnetoelastic coupling with the shear waves in the bulk acoustic resonator formed by the layer stack. The derived magnetoelastic constants are therefore much less sensitive to inhomogeneities and other contributions to the line broadening [12].

## IV. CONCLUSIONS

In summary, our high resolution FMR data taken over a broad frequency range confirm that magnon-phonon coupling in confined systems depends not only on the material parameters, but also qualitatively changes with the mode overlap. This provides the option of tuning the magnon-phonon coupling strength by the frequency, magnetic field variations, and sample geometry. We analyzed the magnon-phonon mode coupling over a broad frequency range by a simple harmonic oscillator model, revealing the oscillating nature of the acoustic spin pumping efficiency as predicted theoretically [3]. Broadband phonon pumping experiments are interesting for studying other material combinations such as $SiO_2$/Py [14] and should allow for assessing the acoustic properties of magnetic phase diagrams, e.g., of the frustrated magnetic phase of GGG at low temperatures [46].

## ACKNOWLEDGMENTS

We would like to acknowledge useful discussions with O. Klein, A. Kamra, P. Noël, and W. Legrand. We acknowledge

financial support by the Deutsche Forschungsgemeinschaft (DFG, German Research Foundation)–Project-id No. 425217212–SFB 1432 and Project-id No. 247310070–SFB 1143, the Würzburg-Dresden Cluster of Excellence on Complexity and Topology in Quantum Matter - ct.qmat (EXC 2147, Project-id No. 39085490), the Cluster of Excellence "Munich Center for Quantum Science and Technology" (EXC 2111, Project-id No. 390814868), and JSPS KAKENHI Grant No. 19H00645.

## APPENDIX A: ALTERNATIVE EVALUATION PROCEDURE

An alternative approach to evaluating the broadband FMR data based on a direct fit to the complex scattering parameter is presented in the following. To directly connect to the coupled resonator model and obtain the coupling strength, the impact of the microwave background signal must be removed before the data can be fit. This is accomplished by numerically differentiating the data as well as the coupled resonator model with respect to the frequency. This method is called derivative divide and was already used in a previous broadband FMR experiment to remove the frequency and magnetic field dependent microwave background (however along the field axis) [47]. A side effect of this preprocessing of the data is that the phonon resonances are enhanced: contributions to $S_{21}$ that vary rapidly in frequency (i.e., the phonon resonances) become more pronounced, while slowly varying contributions (i.e., the microwave background) are suppressed. To initialize the fit, we use the same approach as presented in the main text, i.e., we locate the FMR using a Gaussian fit to $|S_{21}|$ [see gray line in Fig. 5(a)]. In the following, the first two phonon resonances that have a spacing from the Kittel mode $\geqslant$22 MHz are fitted with Lorentzians to determine the initial parameters for $\Delta\omega_\mathrm{p}$ (the spacing between the two phonon resonances), $\omega_{\mathrm{p},0}$ (the resonance frequency of the phonon resonance closest to the FMR line), and the linewidth $\gamma_\mathrm{p}$ of the phonon resonance. We then fit the complex preprocessed data using the differentiated model. The processed data and the fit can be seen in Fig. 5(b). We would like to stress that, while this approach works and produces equivalent results if care is taken, some of the parameters show strong correlations. Consequently, it was not possible to automatically fit all of the experimental data reliably, in particular where the magnetoelastic coupling is weak. We attribute this issue to inhomogeneities in the YIG film along the CPW that lead to the broadening of the FMR and the presence of the first PSSW in the flank of the FMR line, which might lead to additional contributions to the phonon pumping. Nevertheless, in another work, a similar approach produced a very good fit of the complex response around the full FMR line, at least for thick YIG films [30].

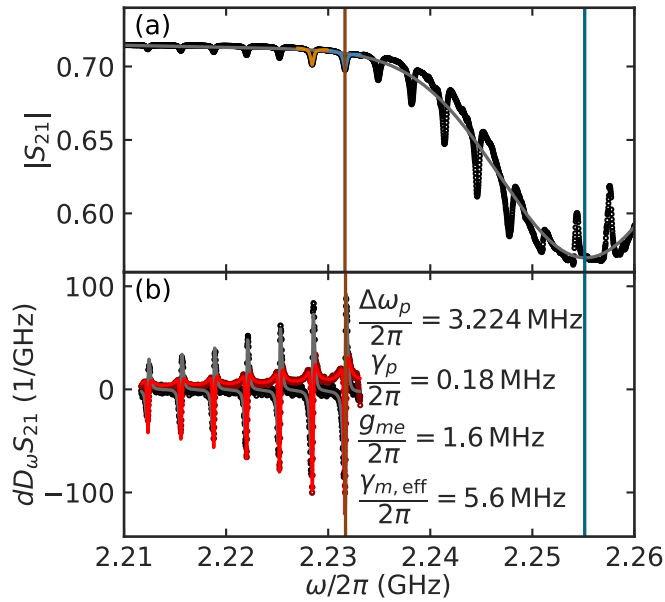


FIG. 5. (a) $|S_{21}|(\omega)$ spectra are used to initialize the fit parameters for fitting the full complex response. In particular, the linewidth of the FMR line $\gamma_\mathrm{m}$ and the phonon resonance $\gamma_\mathrm{p}$ as well as the respective resonance positions $\omega_\mathrm{m}$ and $\omega_\mathrm{p}$ are extracted. (b) $S_{21}$ expected from the model [cf. Eq. (5) in the main text] is differentiated along the frequency axis and the resulting complex $\partial A_\mathrm{m}(\omega)/\partial\omega$ is fitted to a set of seven lines (simultaneously). The black line is the real part, while the red line shows the imaginary part of $S_{21}$. We find good quantitative agreement with the parameters that are extracted using the approach presented in the main text.

## APPENDIX B: FULL SET OF FIT PARAMETERS AND DISCUSSION

In this section we list all of the different parameters that we obtain from our automatic fitting procedure (summarized in Fig. 6) and discuss their physical implications. In particular, the magnitude of the microwave background decays exponentially [panel (a)]. We point out that the dip seen around 4 GHz corresponds to a standing wave forming across the CPW structure, which has a length of ∼4 cm. The height of the magnon resonance [panel (b)] shows a linear increase for increasing frequency. The latter is rooted in the measurement of our signal: $S_{21}$ has a component proportional to the voltage induced into the coplanar waveguide by the precessing magnetization $M(t)$. The inductance between the sample and the CPW is a constant given by the geometry, so that the voltage increases linearly with frequency due to the increase of $\partial M(t)/\partial t$ [48]. As a consequence, also the coupling strength between the CPW and the YIG sample [panel (d)] increases linearly with frequency.

The height of the phonon resonance shown in panel (e) exhibits a clear maximum around 3 GHz, vanishes around 6 GHz, and then has another maximum around 9 GHz. It thus reflects the oscillating nature of the magnetoelastic coupling discussed in the main text. Note that this signature is observed for all the six fitted phonon lines and thus is independent of the distance of the phonon resonance from the FMR line. It is obvious that the amplitude of the phonon resonance depends strongly on the separation from the FMR line. In particular, it roughly scales as the inverse of the separation from the FMR line, so that $h_\mathrm{p}$ is strongly suppressed when increasing the separation. This is taken into account by the model when calculating the coupling strength shown in panel (g). The height of the phonon resonance is the dominant parameter when determining the coupling strength from the resonator model and thus will introduce the largest error.

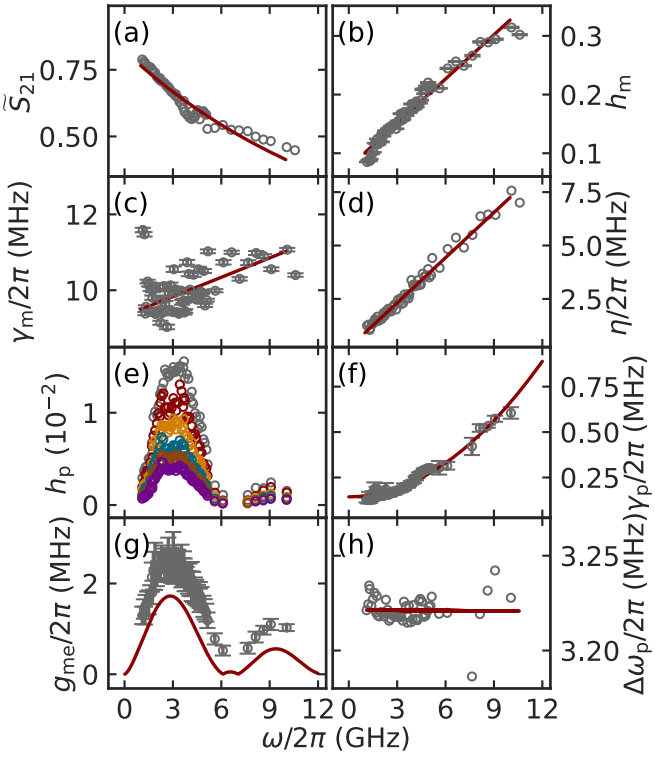


FIG. 6. (a) Absolute microwave transmission of the coplanar waveguide $\widetilde{S}_{21}$ loaded with the sample in the absence of the FMR line decays roughly following an exponential. (b), (c) Amplitude and half width at half maximum (HWHM) obtained from Gaussian fits to the FMR line. (d) The magnon-photon coupling strength between the CPW and the FMR in the YIG film decreases linearly by ∼20 % in the investigated frequency window. (e), (f) Amplitude and width (HWHM) extracted from Lorentzian fits of the acoustic resonances. (g) The magnon-phonon coupling strength that parametrizes the spin pumping process and is discussed in more detail in the main text. (h) The free spectral range of the acoustic resonator does not depend on frequency, suggesting constant speed of sound in the investigated frequency range.

Finally, one other parameter that we can determine from our fitting is the free spectral range, which is directly proportional to the sound velocity [see Eq. (1) in the main text]. The free spectral range is shown in panel (h). For a phonon band with linear dispersion, one expects a constant sound velocity, which is confirmed by our observation of a frequency independent free spectral range for frequencies up to 11 GHz.

## APPENDIX C: ESTIMATION OF THE PHONON AMPLITUDE

To obtain an upper limit for the phonon amplitude, we estimate the absorbed microwave power from the maximum height of the phonon resonances in $|S_{21}|^2$ observed around 3.2 GHz ($\Delta|S_{21}|^2 \sim -0.017$). Assuming all this power is lost within the phononic system, we can estimate an absorbed power of $P_{\text{in}} \sim 54\,\mu\text{W}$ for an applied microwave power of 5 dBm. To recalculate the power into a phonon amplitude, we first assume that this power is distributed over the excited part of the sample. This is defined by the thickness of the layer

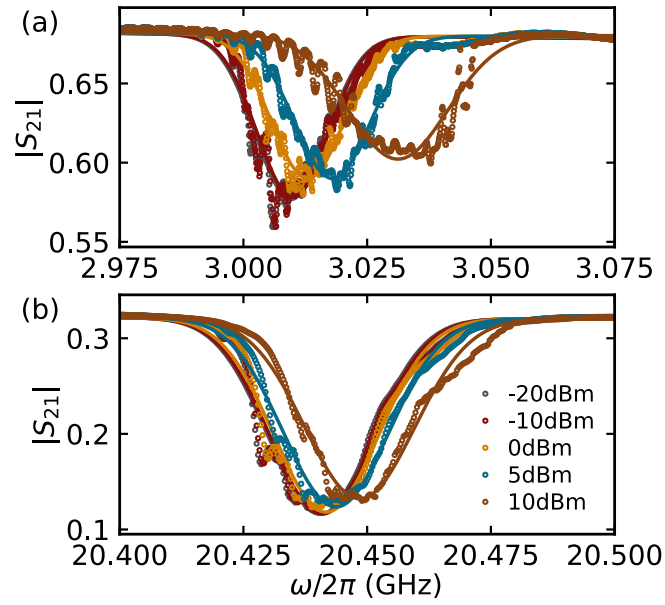


FIG. 7. (a) Absolute microwave transmission as a function of frequency around the ferromagnetic resonance and at the maximum of the magnetoelastic coupling. (b) Same data for a much higher frequency show a much weaker dependence on power due to the reduced microwave transmission of the coplanar waveguide.

stack $t \approx 560\,\mu\text{m}$ and the length of the sample on the CPW $l = 6\,\text{mm}$, as well as the width of the CPW $w = 110\,\mu\text{m}$. Using this volume and the relaxation rate $\gamma_p \sim 200\,\text{kHz}$ of the phonons, we can then estimate the time averaged energy density contained in the mode as

$$E = \frac{P_{\text{in}}}{lwt\gamma_p} = 0.73\,\text{Jm}^{-3}. \tag{C1}$$

In turn, the energy density contained in the phonon mode in relation to its frequency and time-averaged amplitude $x$ is given by $E = \rho\omega^2 x^2/8$ [49], where $\rho$ is the mass density of YIG. Comparing these two energies allows one to estimate a maximum displacement amplitude due to phonon pumping of $x = 1.7\,\text{pm}$.

## APPENDIX D: POWER DEPENDENCE OF THE FERROMAGNETIC RESONANCE AND THE MAGNETOELASTIC COUPLING PARAMETERS

Power dependent measurements of the FMR line are displayed in Fig. 7 for low and high FMR frequency. Before going into the details of the power dependence, we briefly want to discuss the line shape and the associated issues for extracting the intrinsic linewidth. We note that the line is not well described by a Lorentzian, as already pointed out in the main text. As evident from the evolution of the linewidth with frequency shown in Fig. 6(c), the linewidth is dominated by inhomogeneous broadening. We thus associate the shape of the line to a non-Gaussian distribution of the effective magnetization, presumably in different grains within the YIG film. Such a distribution might have an asymmetry in a high quality magnetic thin film, since the upper limit of the saturation magnetization is defined by the bulk value, whereas it can

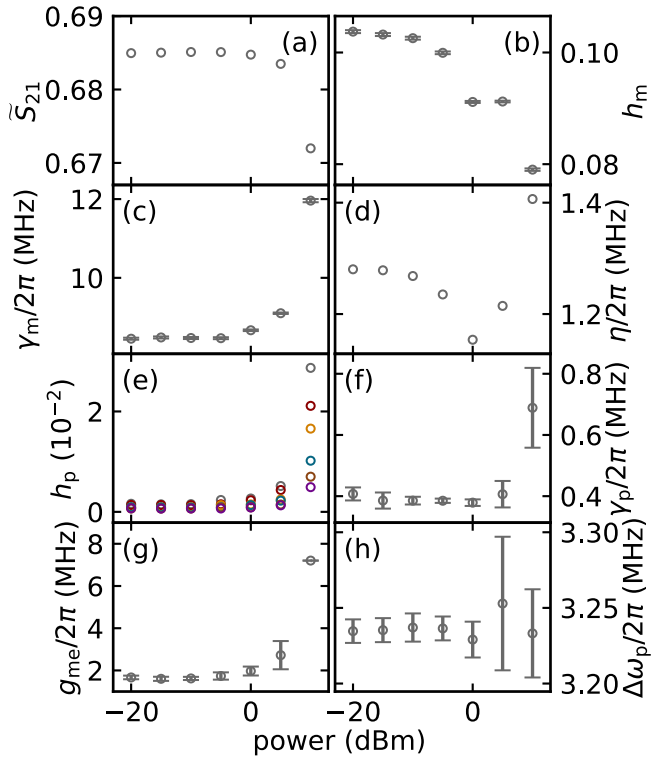


FIG. 8. (a) Background of the absolute microwave transmission of the CPW $\widetilde{S}_{21}$. (b), (c) Amplitude and half width at half maximum (HWHM) obtained from Gaussian fits to the FMR line. (d) The magnon-photon coupling strength varies by ∼20 % with the applied power. (e), (f) Amplitude and width (HWHM) extracted from Lorentzian fits of the acoustic resonances. (g) The magnon-phonon coupling strength does not evolve with power until 5 dBm, above which it sharply increases. (h) The free spectral range of the acoustic resonator is independent of power.

be lowered by grain formation and other defects. As such, the extraction of the intrinsic linewidth is impossible without knowledge of the distribution function, as the resulting line shape is defined by a convolution of the intrinsic Lorentzian shape of each individual grain and the distribution function [50]. We have confirmed that, even at 20 GHz, the shape of the line is still not described by a Lorentzian, suggesting that the inhomogeneous line hinders the extraction of the true intrinsic quality of the YIG film used here. A change of the line shape can enter the fitting results in an ambiguous fashion, depending on the exact line shape used for fitting. Nevertheless, we verified that the power does not affect the extracted Gilbert damping by performing broadband FMR measurements at −20 dBm, which yield the same Gilbert damping as at +5 dBm within 10 % (data not shown). We note that this discussion does not affect the conclusions drawn in the main text, apart from introducing small errors, as an effective linewidth is used for the estimation of the coupling parameters instead of the true linewidth of a single magnetic mode.

At low frequency and for powers below −10 dBm the FMR is not affected by the power. The line starts to shift at a power of 0 dBm and small distortions are visible at 5 dBm, the power that was used in the main text. Shifts of the line are observed when the sample is heated, reducing the saturation magnetization of the YIG layer. We chose a power of 5 dBm to improve the signal to noise ratio, allowing one to resolve the small phonon oscillations with high fidelity and supporting the automated fitting approach presented in the main text. At 10 dBm the response becomes nonlinear and the line broadens and distorts significantly, showing the characteristic onset of the nonlinear foldover regime at the high frequency end of the line [51].

At elevated frequencies [see Fig. 7(b)], the transmission of the CPW is reduced, so that the power transmitted to the sample decreases by ∼3 dB. As such, the line shifts only at powers larger than 5 dBm and no sign of the foldover regime is evident in the data. Note that discontinuities in the line taken at 10 dBm are due to the VNA ports becoming unleveled.

To evaluate the influence of the microwave power and the nonlinearities in the magnetic system on the extracted magnetoelastic coupling, we have repeated the extraction procedure described in the manuscript for the data shown in Fig. 7(a). The resulting parameters are summarized in Fig. 8. We find that the background transmission only changes when the VNA becomes unleveled, i.e., at 10 dBm. Furthermore, the height of the FMR line decreases and its width increases towards higher power, respectively. This is in line with what is reported in literature [51]. We note that the overestimation of the linewidth due to the enhanced power is on the order of 10 % for the power used throughout the main text. In the foldover regime at 10 dBm the magnetoelastic coupling seems to be enhanced, which we associate with the wide range in which the ferromagnetic resonance is driven. However, the model of two coupled harmonic oscillators clearly breaks down in this regime, so that our estimation loses its validity and further theoretical effort must be taken to clarify the expected evolution in this regime. Finally, the extracted magnetoelastic coupling is overestimated by the same 10 % as the linewidth of the FMR line for the 5 dBm used in the main text. We conclude that the fitting method provides robust results and that the power only weakly affects the extracted parameters as long as the system remains in the linear regime (powers up to 5 dBm in our case).

## APPENDIX E: THICKNESS DEPENDENCE OF THE MAGNETOELASTIC COUPLING

To further confirm the predictions of the theory [2,3], we have repeated the measurements shown in the main text for samples with different YIG thicknesses of $t_{YIG} = 1$ and 2 µm [see Figs. 9(a), 9(b) and 9(c), 9(d), respectively]. The measurements on both samples reveal the same salient features as the sample that is discussed in the main text. In particular, the magnetoelastic coupling seen as the horizontal interruptions of the FMR periodically appears and disappears, following a characteristic oscillation. To confirm that it matches with the model proposed in the main text, the expected magnetoelastic coupling for the two thicknesses is shown in panels (b) and (d). Very good qualitative agreement with the theoretical expectation [given by Eq. (4) in the main text] is found, which further corroborates the proposed coupling mechanism and the generality of the observed magnetoelastic coupling. A full extraction of the coupling parameters in these samples is challenging, as the FMR line

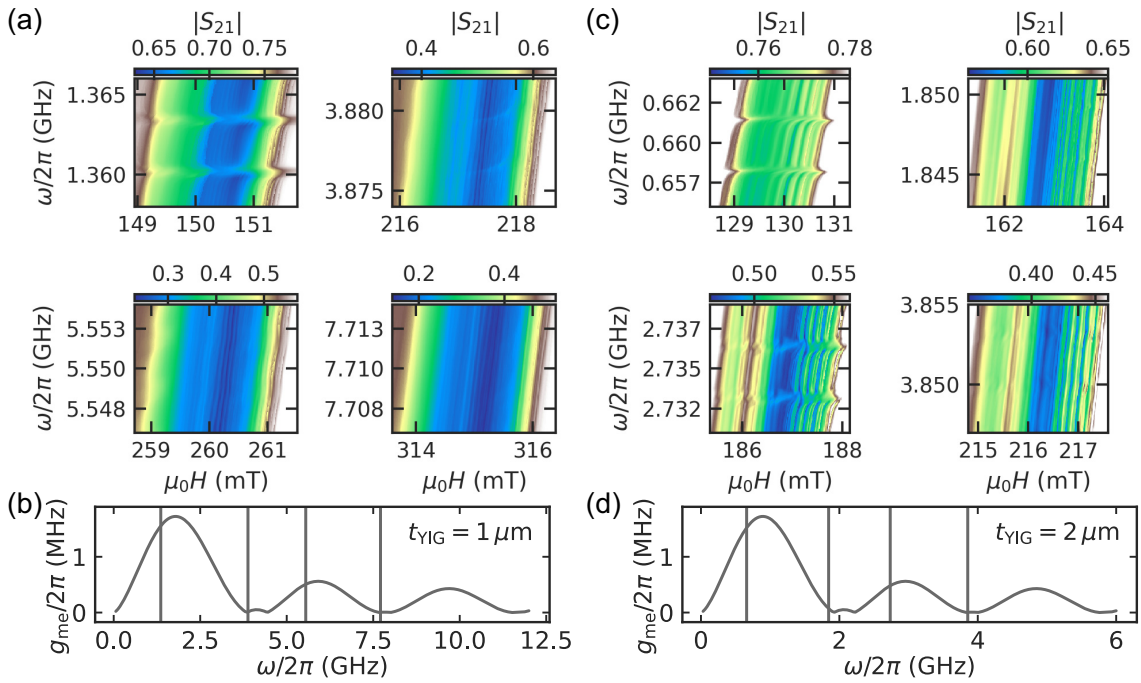


FIG. 9. (a), (c) $|S_{21}|$ maps of samples with YIG thickness of 1 μm and 2 μm, respectively. The magnetoelastic coupling (seen as periodic anticrossings) periodically disappears when the FMR frequency is varied. (b), (d) Expected magnetoelastic coupling strength as a function of frequency according to Eq. (4) in the main text. The vertical lines denote the frequencies at which the maps were taken.

consists of multiple modes. This is more problematic for higher YIG thicknesses, as the PSSWs reside closer to the main FMR line [32], so that their contribution to the magnetoelastic coupling cannot be disregarded.


[1] F. Godejohann, A. V. Scherbakov, S. M. Kukhtaruk, A. N. Poddubny, D. D. Yaremkevich, M. Wang, A. Nadzeyka, D. R. Yakovlev, A. W. Rushforth, A. V. Akimov, and M. Bayer, Phys. Rev. B **102**, 144438 (2020).

[2] T. Sato, W. Yu, S. Streib, and G. E. W. Bauer, Phys. Rev. B **104**, 014403 (2021).

[3] S. Streib, H. Keshtgar, and G. E. W. Bauer, Phys. Rev. Lett. **121**, 027202 (2018).

[4] K. An, A. N. Litvinenko, R. Kohno, A. A. Fuad, V. V. Naletov, L. Vila, U. Ebels, G. de Loubens, H. Hurdequint, N. Beaulieu, J. Ben Youssef, N. Vukadinovic, G. E. W. Bauer, A. N. Slavin, V. S. Tiberkevich, and O. Klein, Phys. Rev. B **101**, 060407(R) (2020).

[5] A. Rückriegel and R. A. Duine, Phys. Rev. Lett. **124**, 117201 (2020).

[6] J. Holanda, D. S. Maior, O. A. Santos, A. Azevedo, and S. M. Rezende, Appl. Phys. Lett. **118**, 022409 (2021).

[7] S. M. Rezende, D. S. Maior, O. Alves Santos, and J. Holanda, Phys. Rev. B **103**, 144430 (2021).

[8] J. Graf, S. Sharma, H. Huebl, and S. V. Kusminskiy, Phys. Rev. Research **3**, 013277 (2021).

[9] K. An, R. Kohno, A. N. Litvinenko, R. L. Seeger, V. V. Naletov, L. Vila, G. de Loubens, J. Ben Youssef, N. Vukadinovic, G. E. W. Bauer, A. N. Slavin, V. S. Tiberkevich, and O. Klein, Phys. Rev. X **12**, 011060 (2022).

[10] A. V. Chumak and H. Schultheiss, J. Phys. D **50**, 300201 (2017).

[11] A. V. Chumak, P. Kabos, M. Wu, C. Abert, C. Adelmann, A. Adeyeye, J. Åkerman, F. G. Aliev, A. Anane, A. Awad, C. H. Back, A. Barman, G. E. W. Bauer, M. Becherer, E. N. Beginin, V. A. S. V. Bittencourt, Y. M. Blanter, P. Bortolotti, I. Boventer, D. A. Bozhko *et al.*, IEEE Trans. Magn. **58**, 1 (2022).

[12] V. Cherepanov, I. Kolokolov, and V. L'vov, Phys. Rep. **229**, 81 (1993).

[13] T. Gilbert, IEEE Trans. Magn. **40**, 3443 (2004).

[14] M. Pomerantz, Phys. Rev. Lett. **7**, 312 (1961).

[15] H. Matthews and R. C. LeCraw, Phys. Rev. Lett. **8**, 397 (1962).

[16] C. F. Kooi, Phys. Rev. **131**, 1070 (1963).

[17] P. M. Rowell, Br. J. Appl. Phys. **14**, 60 (1963).

[18] C. F. Kooi, P. E. Wigen, M. R. Shanabarger, and J. V. Kerrigan, J. Appl. Phys. **35**, 791 (1964).

[19] P. E. Wigen, W. I. Dobrov, and M. R. Shanabarger, Phys. Rev. **140**, A1827 (1965).

[20] T. Kobayashi, R. C. Barker, and A. Yelon, Phys. Rev. B **7**, 3286 (1973).

[21] Y. Sunakawa, S. Maekawa, and M. Takahashi, J. Magn. Magn. Mater. **46**, 131 (1984).

[22] K. Uchida, J. Xiao, H. Adachi, J. Ohe, S. Takahashi, J. Ieda, T. Ota, Y. Kajiwara, H. Umezawa, H. Kawai, G. E. W. Bauer, S. Maekawa, and E. Saitoh, Nat. Mater. **9**, 894 (2010).

[23] M. Bombeck, A. S. Salasyuk, B. A. Glavin, A. V. Scherbakov, C. Brüggemann, D. R. Yakovlev, V. F. Sapega, X. Liu, J. K. Furdyna, A. V. Akimov, and M. Bayer, Phys. Rev. B **85**, 195324 (2012).

[24] T. Kikkawa, K. Shen, B. Flebus, R. A. Duine, K. I. Uchida, Z. Qiu, G. E. W. Bauer, and E. Saitoh, Phys. Rev. Lett. **117**, 207203 (2016).
[25] M. Goryachev, S. Galliou, and M. E. Tobar, Phys. Rev. B **100**, 174108 (2019).
[26] K. Harii, Y.-J. Seo, Y. Tsutsumi, H. Chudo, K. Oyanagi, M. Matsuo, Y. Shiomi, T. Ono, S. Maekawa, and E. Saitoh, Nat. Commun. **10**, 2616 (2019).
[27] M. Goryachev, S. Galliou, and M. E. Tobar, Phys. Rev. Research **2**, 023035 (2020).
[28] N. K. P. Babu, A. Trzaskowska, P. Graczyk, G. Centała, S. Mieszczak, H. Głowiński, M. Zdunek, S. Mielcarek, and J. W. Kłos, Nano Lett. **21**, 946 (2021).
[29] A. Litvinenko, R. Khymyn, V. Tyberkevych, V. Tikhonov, A. Slavin, and S. Nikitov, Phys. Rev. Appl. **15**, 034057 (2021).
[30] S. N. Polulyakh, V. N. Berzhanskii, E. Y. Semuk, V. I. Belotelov, P. M. Vetoshko, V. V. Popov, A. N. Shaposhnikov, A. G. Shumilov, and A. I. Chernov, J. Exp. Theor. Phys. **132**, 257 (2021).
[31] C. Dubs, O. Surzhenko, R. Thomas, J. Osten, T. Schneider, K. Lenz, J. Grenzer, R. Hübner, and E. Wendler, Phys. Rev. Materials **4**, 024416 (2020).
[32] C. Kittel, Phys. Rev. **110**, 1295 (1958).
[33] J. T. Yu, R. A. Turk, and P. E. Wigen, Phys. Rev. B **11**, 420 (1975).
[34] F. Schreiber and Z. Frait, Phys. Rev. B **54**, 6473 (1996).
[35] S. Klingler, A. V. Chumak, T. Mewes, B. Khodadadi, C. Mewes, C. Dubs, O. Surzhenko, B. Hillebrands, and A. Conca, J. Phys. D **48**, 015001 (2015).
[36] M. Ye and H. Dötsch, Phys. Rev. B **44**, 9458 (1991).
[37] R. L. Comstock and R. C. LeCraw, J. Appl. Phys. **34**, 3022 (1963).
[38] M. Ye, A. Brockmeyer, P. E. Wigen, and H. Dötsch, J. Phys. Colloq. **49**, C8-989 (1988).
[39] S. Probst, F. B. Song, P. A. Bushev, A. V. Ustinov, and M. Weides, Rev. Sci. Instrum. **86**, 024706 (2015).
[40] C. Dubs, O. Surzhenko, R. Linke, A. Danilewsky, U. Brückner, and J. Dellith, J. Phys. D **50**, 204005 (2017).
[41] Y.-H. Rao, H.-W. Zhang, Q.-H. Yang, D.-N. Zhang, L.-C. Jin, B. Ma, and Y.-J. Wu, Chin. Phys. B **27**, 086701 (2018).
[42] M. Dutoit and D. Bellavance, *1972 Ultrasonics Symposium* (IEEE, New York, 1972).
[43] M. Dutoit, J. Appl. Phys. **45**, 2836 (1974).
[44] B. C. Daly, K. Kang, Y. Wang, and D. G. Cahill, Phys. Rev. B **80**, 174112 (2009).
[45] M. Krzesińska and T. Szuta-Buchacz, Phys. Status Solidi A **82**, 421 (1984).
[46] P. P. Deen, O. Florea, E. Lhotel, and H. Jacobsen, Phys. Rev. B **91**, 014419 (2015).
[47] H. Maier-Flaig, S. T. B. Goennenwein, R. Ohshima, M. Shiraishi, R. Gross, H. Huebl, and M. Weiler, Rev. Sci. Instrum. **89**, 076101 (2018).
[48] M. A. W. Schoen, J. M. Shaw, H. T. Nembach, M. Weiler, and T. J. Silva, Phys. Rev. B **92**, 184417 (2015).
[49] C. Kittel, *Introduction to Solid State Physics* (Wiley, New York, 2004).
[50] Z. Kurucz, J. H. Wesenberg, and K. Mølmer, Phys. Rev. A **83**, 053852 (2011).
[51] D. J. Seagle, S. H. Charap, and J. O. Artman, J. Appl. Phys. **57**, 3706 (1985).